processes

MDPI

Article

The Flow Performance of Combined Gas Blowing at the Vacuum Chamber and Up-Snorkel in the Ruhrstahl–Heraeus (RH) Degasser for Electrical Steel Production

Liqiang Xue [1,2], Yansong Zhao [1], Jia Wang [1,3,*], Huan Wang [1,4], Zheng Miao [1], Ruixiang Xiong [1], Zhibo Xu [1,2], Wanming Lin [1], Xiaofeng Niu [1] and Chao Chen [1,*]

[1] College of Materials Science and Engineering, Taiyuan University of Technology, Taiyuan 030024, China; xueliqiang421@sina.com (L.X.); zhaoyansong513@163.com (Y.Z.); m202211318@xs.ustb.edu.cn (H.W.); mz15135858598@163.com (Z.M.); 13027221778@163.com (R.X.); 15735511012@163.com (Z.X.); linwanming@tyut.edu.cn (W.L.); niuxiaofeng@tyut.edu.cn (X.N.)
[2] Steelmaking Plant, Shanxi Taigang Stainless Steel Co., Ltd., Taiyuan 030030, China
[3] College of Architecture and Arts, Taiyuan University of Technology, Taiyuan 030024, China
[4] State Key Laboratory of Advanced Metallurgy, University of Science and Technology Beijing, Beijing 100083, China
* Correspondence: wangjia01@tyut.edu.cn (J.W.); chenchao@tyut.edu.cn (C.C.)

Abstract: In the production process of electrical steel, with respect to the industrial RH (Ruhrstahl–Heraeus), the steel producers must balance the high-circulation flow rate (operating efficiency) and the frequent cleaning of cold steel in the vacuum chamber due to the splashing of liquid steel (high maintenance costs). Excessive lifting gas flow can induce splashing, causing cold steel to adhere to the inner walls of the vacuum chamber. To address this issue, this study utilized an 80-ton RH vacuum refining unit from a specific plant as the research prototype and established a 1:2.6 scale water model for physical model simulation. Two innovative blowing methods were implemented by adding gas injection nozzles to the sidewalls and to the bottom of the vacuum chamber, respectively. The study investigated the effects of altering the blowing method on liquid surface fluctuations, flow patterns, the circulation flow rate, and the mixing time without changing the total gas flow rate. For the macroscopic flow in the RH unit, implementing side-blowing on the sidewalls of the vacuum chamber can accelerate the diffusion rate of the ink tracer, whereas implementing bottom-blowing in the vacuum chamber has little effect on the diffusion rate. The results show that modifying the blowing method can effectively reduce liquid surface fluctuations and suppress the splashing behavior within the vacuum chamber. Firstly, implementing side-blowing causes the ink tracer flow pattern within the vacuum chamber to become triangular, to increase the circulation flow rate, to shorten the residence time of the ink tracer within the chamber, and simultaneously to promote mixing in the ladle, which reduces the mixing time. Secondly, implementing bottom-blowing results in the formation of a gas column at the center of the vacuum chamber, which suppresses fluid flow within the chamber. Compared with side-blowing, it reduces the circulation flow rate and increases the mixing time in the ladle. Combined gas blowing through the up-snorkel and sidewalls is effective in solving splashing issues and reducing the mixing time in RH vacuum refining, and this method is a good candidate for industrial applications.

Keywords: RH vacuum refining; splashing phenomenon; physical model; gas injection methods; side-blowing; bottom-blowing

check for updates

Academic Editor: Massimo Caruso

Received: 6 January 2025
Revised: 31 January 2025
Accepted: 5 February 2025
Published: 7 February 2025

Citation: Xue, L.; Zhao, Y.; Wang, J.; Wang, H.; Miao, Z.; Xiong, R.; Xu, Z.; Lin, W.; Niu, X.; Chen, C. The Flow Performance of Combined Gas Blowing at the Vacuum Chamber and Up-Snorkel in the Ruhrstahl–Heraeus (RH) Degasser for Electrical Steel Production. *Processes* **2025**, *13*, 448. https://doi.org/10.3390/pr13020448

Copyright: © 2025 by the authors. Licensee MDPI, Basel, Switzerland. This article is an open access article distributed under the terms and conditions of the Creative Commons Attribution (CC BY) license (https://creativecommons.org/licenses/by/4.0/).

1. Introduction

In recent years, the market for sustainable new energy Electrical Vehicles (EVs) has been progressively expanding. Notably, high-quality electrical steel materials have been extensively utilized in the EV industries [1–4], with escalating demands for electrical steel grades and improved quality [5–7]. For the production of electrical steel, the Basic Oxygen Furnace (BOF)-Ruhrstahl–Heraeus (RH) vacuum refining–continuous casting has become a normal production route in many steelmaking plants [8–12].

The RH vacuum refining integrates multiple functions, including decarburization [13–17], degassing [18], powder injection [19–23], desulfurization [24–26], temperature compensation, homogenization of the composition [27–29], and inclusion removal [30–34]. This technology offers a range of advantages, such as short processing cycles, excellent refining performance, and the capacity to handle large volumes of molten steel. Consequently, RH vacuum refining has become the most critical secondary refining technology for producing high-quality steel. The refining effectiveness within an RH unit is closely related to the flow and mixing of the molten steel. The circulation flow rate and homogenization time are pivotal indicators for evaluating the operational efficiency of RH vacuum refining units and have consistently garnered significant attention from researchers [35–40].

In the industrial refining process, under a large gas flow rate operation condition, the liquid steel on the up-snorkel side of the vacuum chamber will be driven to a high position by bubbles, and a serious splashing of the steel will be formed. As a result, a large portion of liquid steel is adhered to the wall of the vacuum chamber. In the subsequent production processes, it is highly likely to cause problems such as a re-carbonization of the decarburized liquid steel and a blockage of the oxygen lance and alloy chute in the chamber [41]. After a production cycle, the cold steel in the wall of the vacuum chamber needs to be cleaned regularly by burning by an oxygen lance [42]. The frequent cleaning of cold steel will firstly shorten the usage cycle of the RH vacuum chamber and in addition increases the operation and maintenance costs seriously. How to alleviate the splashing phenomenon of liquid steel in the vacuum chamber and effectively improve the operating efficiency of RH vacuum refining equipment is an important issue in production.

Since the inception of RH (Ruhrstahl–Heraeus) refining technology in the 1960s, numerous researchers have employed methods such as water model experiments [43–51], numerical simulations [52–57], and industrial measurements [58] to study the flow behavior of molten steel inside the RH. Researchers can apply these methods to identify the factors affecting the refining efficiency, and then to improve the RH process to enhance its efficiency. The studied factors primarily encompass system geometry and operating conditions. Geometric considerations include the diameter and number of snorkels, the diameter of the vacuum chamber, and the positioning of nozzles. Operating conditions involve argon gas flow rate, vacuum chamber pressure, and the immersion depth of the snorkels.

There are some innovations regarding the new structures change in RH systems, such as changing the shape of the snorkel, adding weirs at the bottom of the vacuum chamber, and changing or implementing gas blowing in the RH system to improve the operating efficiency. It is noted that a large number of researches are focused on the reshape of the two snorkels in RH to a single snorkel, and gas stirring is performed at the bottom of the ladle. This Single Snorkel Refining Furnace technology [59] is not discussed in this paper. Researchers designed an elliptical shape of a snorkel [60,61], and it can increase the circulation flow rate in the RH degasser by 45~218%, and the mixing time is reduced. As a result, the impact and erosion on the bottom and sidewalls of the ladle are weakened. In a recent study, He et al. [62] designed a weir at the bottom of the vacuum chamber. The application of a weir is inspired from the idea of tundish designs [63–65].

The changing or implementing of gas blowing in the RH system consists of (1) a combination of gas blowing at the bottom of ladle [66–69] (corresponding to the location of the up-snorkel); (2) a combination of an argon injection through the down-snorkel [70,71]; (3) implementing gas blowing at the sidewall of vacuum chamber [72,73]; (4) implementing gas blowing at the bottom of vacuum chamber [74]; and (5) changing the layout of the nozzles [75,76] and inclination angles of the nozzles [77,78] in the up-snorkel.

The implementation of gas blowing in the vacuum chamber seems to be a good way to alleviate the splashing phenomenon of liquid steel in the vacuum chamber. In possibly the earliest study, Inoue et al. [72] argued that increasing the inner diameter of a snorkel is not commonly adopted in industry. They installed 1, 8, or 16 nozzles at the lowest part of the vacuum chamber sidewall to study the impact of increasing side-blowing on the decarburization rate. Their research found that increasing side-blowing enlarges the interfacial area, thereby enhancing the decarburization rate. Industrial trials confirmed that the decarburization rate for ultra-low carbon steel increased most significantly, without affecting the circulation flow rate and the slag accumulation within the vacuum chamber. Zheng et al. [73] proposed implementing nozzles to the sidewall in order to improve the utilization of the powder and reduce splashing from the top lance. They aimed to identify the optimal blowing positions for the maximum circulation flow rate and shortest mixing time, and so they implemented five blowing holes on the sidewall of the vacuum chamber. They concluded that the optimal blowing positions vary under different gas injection rates and different lifting gas flow rates. Neves et al. [74] arranged 12 nozzles around the up-snorkel at the bottom of the vacuum chamber and discovered that increasing bottom-blowing can improve decarburization efficiency. However, because the gas is injected around the entire perimeter of the up-snorkel, it restricts the flow within the vacuum chamber, resulting in a decrease in the circulation flow rate.

While extensive research has been conducted on the factors affecting the refining efficiency of traditional RH units, only a few researchers have proposed implementing gas blowing at the sidewalls or bottom of the vacuum chamber [72–74]. However, studies on side-blowing have employed gas flow rates significantly higher than those used for up-snorkel blowing [73]. Additionally, research on bottom-blowing has primarily focused on its advantages in decarburization rates. Comprehensive investigations into the effects of gas injection in the sidewalls or bottom of the vacuum chamber on circulation efficiency and splashing issues are the main motivation of this study.

This research establishes a physical model based on the 80-ton RH unit prototype. The study investigates the impact of injecting gas into the sidewalls and bottom of the vacuum chamber on the circulation flow rate, mixing time, and liquid splashing within the vacuum chamber. The objective is to provide a theoretical foundation for optimizing the operation of actual RH refining equipment, thereby improving efficiency and reducing the splashing related maintenance costs.

2. Experimental Principle and Scheme

2.1. Experimental Principle

In previous studies, the maximum geometric similarity ratio of the RH water model was 1:3 [49], and the minimum similarity ratio was 1:20 [79]. It is believed that the larger the geometric similarity ratio, the more accurate the physical simulation results will be. This experiment utilized an 80-ton RH (Ruhrstahl–Heraeus) vacuum refining unit from a steel plant as the prototype to establish a physical model with a geometric similarity ratio of 1:2.6. The parameters of both the prototype and the model are presented in Table 1. As shown in Figure 1, the water model apparatus is primarily constructed from acrylic glass, while other equipment includes a supporting frame made by steels, a vacuum pump, gas

compressor, rubber hoses, and U-tube manometers. Water at 20 °C was used to simulate molten steel, and compressed air was employed to simulate argon gas in the physical simulation experiments [45]. Both the water and air are iso-thermal.

Table 1. Model and prototype size parameters.

Name of Parameter	Prototype (mm)	Model (mm)
Ladle height	2759.6	1061.4
Upper ladle diameter	2470.6	950.2
Lower ladle diameter	2130.6	819.5
Vacuum chamber diameter	1350	519.2
Snorkel length	1040	400
Up-snorkel/down-snorkel inner diameter	350	134.6

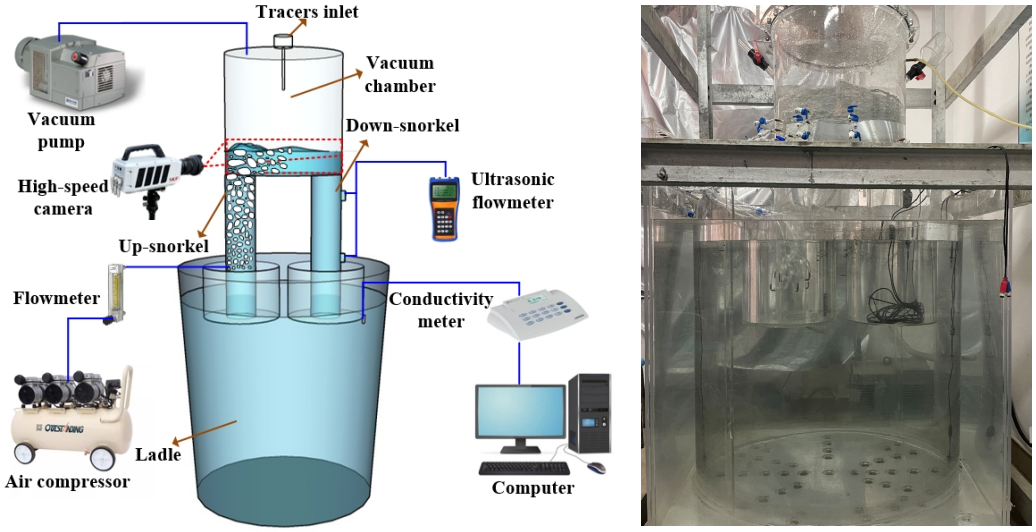


Figure 1. Water model experimental installation; (**a**) schematic diagram; and (**b**) real picture.

In physical simulations, it is essential not only to ensure geometric similarity between the experiment and the prototype but also to ensure that the Reynolds number (Re) and Froude number (Fr) of both the model and the prototype are equal. Since the Reynolds numbers in the down-snorkel of both the model and the prototype all exceed 10^4, placing them in the turbulent flow region, it is sufficient to ensure an equal amount of the Froude numbers to achieve dynamic similarity [39].

$$\mathrm{Fr} = \frac{\rho_{g,p} {u_p}^2}{g D_p \left(\rho_{l,p} - \rho_{g,p}\right)} = \frac{\rho_{g,m} {u_m}^2}{g D_m \left(\rho_{l,m} - \rho_{g,m}\right)} \tag{1}$$

The relationship between Q_m and Q_p are derived by ensuring that Fr numbers are equal, as follows:

$$\frac{Q_m}{Q_p} = \sqrt{\frac{\rho_{g,p}}{\rho_{g,m}} \frac{\left(\rho_{l,m} - \rho_{g,m}\right)}{\left(\rho_{l,p} - \rho_{g,p}\right)} \left(\frac{D_m}{D_p}\right)^5} \tag{2}$$

where D is the geometric characteristic parameter, m; g is the gravitational acceleration, m^2/s; u is the nozzle velocity, m/s; ρ_g is the gas density, kg/m^3; and ρ_l is the liquid density, kg/m^3. Subscripts m and p represent the water model and prototype, respectively. The physical properties are presented in Table 2.

Table 2. Physical property parameters.

Materials	ρ/(kg·m^{-3})	μ/(Pa·s)	Working Temperature/K	Lifting Gas Pressure/MPa
Air	1.184	1.86×10^{-5}	298	0.6
Argon Gas	1.782	2.22×10^{-5}	298	2.5
Molten Steel	7000	6.1×10^{-3}	1873	-
Water	1000	0.89×10^{-3}	298	-

It is also important to ensure that the pressure differences of the model and prototype are identical [39].

$$\frac{\Delta P_m}{\Delta P_p} = \frac{P_0 - P_m}{P_0 - P_p} = \frac{\rho_m g H_m}{\rho_p g H_p} \quad (3)$$

Here, ΔP is the vacuum degree. H is the height difference between the liquid level in the vacuum chamber and the liquid level in the ladle, m.

2.2. Experimental Scheme

Figure 2 provides a schematic diagram of the locations of the gas injection nozzles. The nozzles are installed at a height of 37 mm on the sidewall of the vacuum chamber and at the center of the bottom. Zheng et al. [73] found that the circulation flow rate is higher when the side-blowing position is at a 45-degree angle. Thus, in this study, the nozzle on the sidewall is arranged horizontally, with the lines connecting the nozzle to the center of the vacuum chamber forming a 45° angle relative to the lines connecting the up-snorkel to the center of the vacuum chamber. At the bottom, vertical porous plugs are used, and the diameters of the gas injection holes are consistent with those of the holes in the up-snorkel.



Figure 2. Schematic diagram of the vacuum chamber nozzle location. (**a**) Sidewall and (**b**) bottom.

In this experiment, the following four operating conditions were designed as follows: (1) a gas flow rate at the up-snorkel at 25 L/min; (2) a gas flow rate at the up-snorkel at 45 L/min; (3) a gas flow rate at the up-snorkel at 25 L/min + gas flow rate at the sidewall of the vacuum chamber at 20 L/min (the nozzle position is close to the up-snorkel, positioned at a 45-degree angle relative to it, and 37 mm from the bottom of the vacuum chamber); and (4) a gas flow rate at the up-snorkel at 25 L/min + gas flow rate at the central of the vacuum chamber bottom at 20 L/min. The detailed cases are summarized in Table 3. According to Equation (2), the flow rate in water models 25, 20, and 45 L/min correspond to the 625, 500, and 1125 L/min in industrial operations.

Table 3. The studied cases.

Cases	Gas Blowing Method and Flow Rate
Case 1	Up-snorkel only 25 L/min
Case 2	Up-snorkel only 45 L/min
Case 3	Up-snorkel 25 L/min + sidewall at the vacuum chamber 20 L/min
Case 4	Up-snorkel 25 L/min + bottom wall at the vacuum chamber 20 L/min

2.3. Experimental Methods

The evaluation metrics for assessing the flow conditions within the apparatus include liquid level fluctuation, the tracer mixing process, circulation flow rate, and the tracer mixing time within the ladle. The following experiments were conducted on the physical model. All experiments need to be measured after the flow has stabilized.

2.3.1. Ladle and Vacuum Chamber Flow Visualization

During the experiment, the vacuum pump was first activated. Once a sufficient volume of liquid had risen into the vacuum chamber, the gas valve was opened to initiate gas blowing. After the overall liquid flow within the experimental setup stabilized and the height difference in the manometer pressure gauge reached equilibrium, the ink tracer was rapidly introduced through the tracer inlet at the top of the vacuum chamber, as shown in Figure 1a. A camera was used to record the movement trajectory of the tracer within the apparatus, facilitating the observation and analysis of the flow state within the ladle and vacuum chamber.

For the visualization of the gas injection in the vacuum chamber, followed by the method of Li et al. [80], a 5 mL ink tracer was injected from a syringe at the nozzles in the vacuum chamber. Due to the difference of the flow patterns of side and bottom-blowing, both the injection of the ink at the sidewall nozzle and bottom nozzle was performed. The injection position is shown in Figure 3.

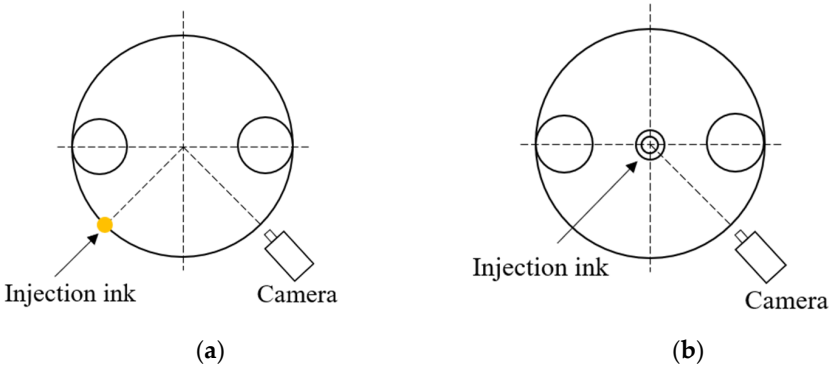


Figure 3. Schematic diagram of the vacuum chamber injection location. (**a**) Sidewall and (**b**) bottom.

2.3.2. Circulation Flow Rate Measurement

The circulation flow rate within the apparatus was determined by measuring the volumetric flow rate of the liquid in the down-snorkel. A TDS-100H handheld ultrasonic flow meter (Xiangjin Flow Meter Factory, Taizhou, China) was employed, with two ultrasonic sensors installed in the down-snorkel. As ultrasonic beams propagate through the liquid, the flow induces slight variations in the propagation time, which are proportional to the liquid velocity. Once the flow within the apparatus stabilized, the flow meter was activated to record the volumetric flow rate in the down-snorkel. Due to the potential presence of minor air bubbles causing significant fluctuations in flow velocity, measurements were taken every second. Ten data points were averaged to determine the mean circulation flow rate for each experimental period.

2.3.3. Liquid Surface Fluctuations in the Vacuum Chamber

After achieving a stable operating condition, a FuHuang AgileDevice Revealer 5KF20SM 3000 fps high-speed camera (HF Agile Device Co., Ltd., Hefei, China) was utilized to record the flow state of the liquid within the vacuum chamber. The recorded footage was subsequently processed to determine the fluctuation height of the liquid surface.

2.3.4. Mixing Time Measurement

The mixing time was measured using the stimulus–response method. Once the flow state within the RH physical model apparatus stabilized, 200 mL of saturated NaCl solution was injected rapidly at the top center of the vacuum chamber. Electrode probes were placed at designated measurement points as shown in Figure 4, and a computer recorded the changes in electrical conductivity at these points. The recorded data were then non-dimensionalized to determine the mixing time at each measurement point. To ensure the accuracy of the experimental data, each set of experiments was repeated ten times, and the average value was taken as the final result.

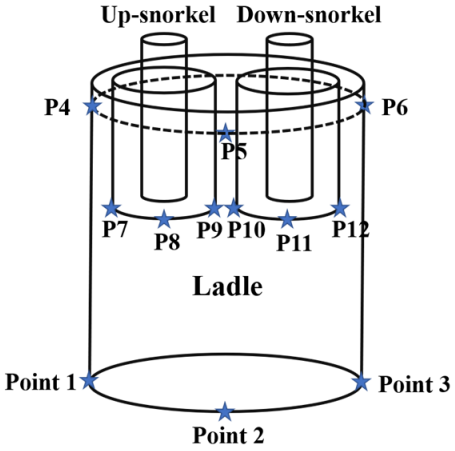


Figure 4. Schematic diagram of monitoring points.

3. Results

3.1. Flow Visualization Experiment

3.1.1. Flow in RH Unit

A computational fluid dynamics (CFD) model result on the streamline in the RH (case 2) is shown in Figure 5. The modeling strategy, mesh test, simulation software STAR CCM+ (17.02.007-R8), and validation is similar to our previous work [39]. Thus, since those CFD results are not the main focus in this study, the simulation details are not presented here. It can be seen that a small part of liquid flows upward through the anticlockwise circulation on the right side of the descending stream, and a major portion of the liquid flows upward through the clockwise circulation on the left side of the descending stream. Finally, the fluid flows back to the vacuum chamber through the up-snorkel. This flow pattern has been reported by many researchers.

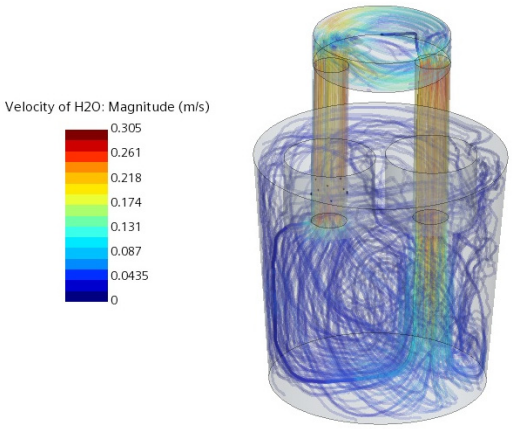


Figure 5. Prediction results of the streamline in the RH water model.

Figure 6 presents the water model visualization results of the ink diffusion within the RH device under four different operating conditions. As clearly shown in Figure 6a, the flow from the down-snorkel reaches the bottom of the ladle and primarily diffuses in two directions thereafter. A large portion of the ink flows leftward along the bottom of the ladle, continuously moving upward throughout the entire ladle. A smaller portion adheres to the right wall of the ladle, steadily ascending and diffusing. Overall, the flow within the RH ladle spreads from the bottom on the down-snorkel side to the upper part on the opposite side. Among the four conditions, the lifting gas flow rate of 45 L/min (case 2) resulted in the fastest ink diffusion, with the ink nearly filling the entire ladle within 20 s. The next fastest condition was the lifting gas flow rate of 25 L/min combined with a side-blowing rate of 20 L/min (case 3). In this scheme, some gas is injected from the vacuum chamber sidewall, and the action of bubbles accelerates the diffusion speed. The ink had completely filled the entire bottom of the ladle within 8 s and reached the up-snorkel position by 20 s. Compared to the condition with the life gas flow rate of 25 L/min alone (case 1), increasing the side-blowing in the vacuum chamber sidewall will enhance the rate of ink diffusion, whereas increasing the bottom-blowing at the vacuum chamber has little effect. Therefore, under the condition of a 25 L/min lifting gas flow rate, increasing the side-blowing in the vacuum chamber effectively promotes the mixing of the liquid within the ladle.

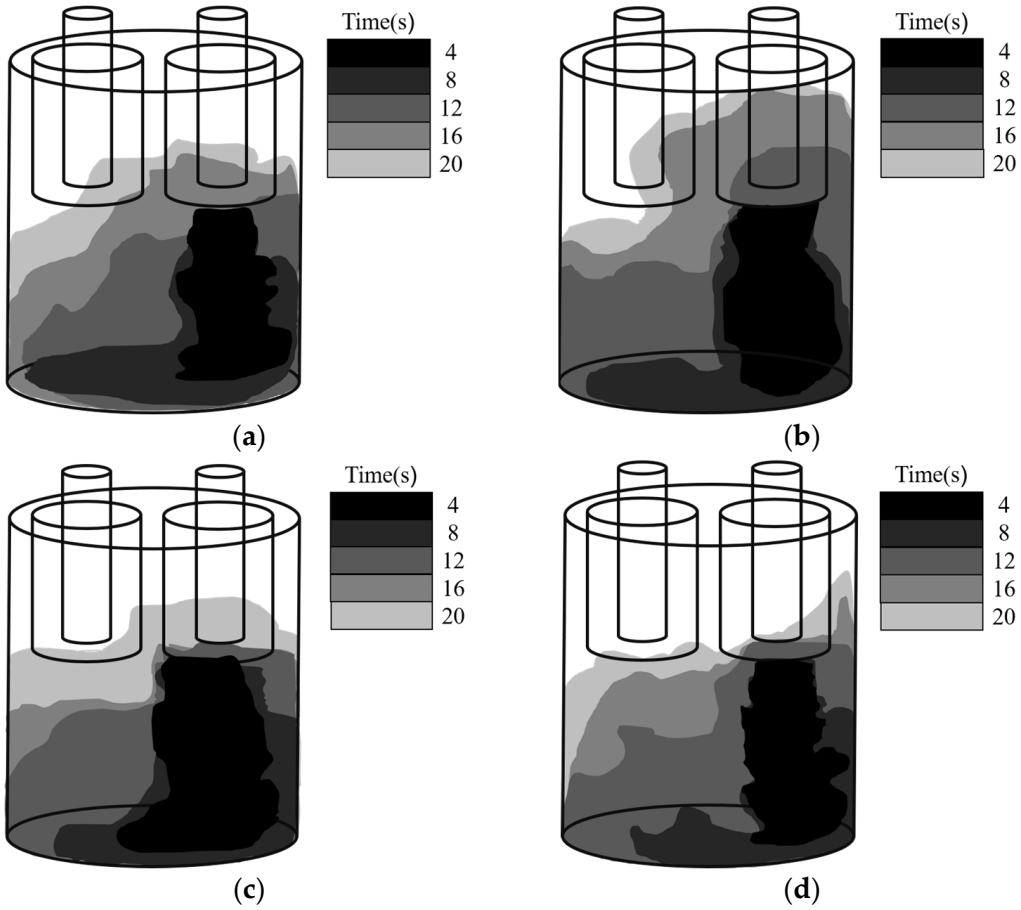


Figure 6. Ink visualization results under four working conditions: (**a**) 25 L/min, (**b**) 45 L/min, (**c**) side-blowing, and (**d**) bottom-blowing.

3.1.2. Flow Visualization After Injection of the Ink from the Nozzle at the Sidewall of the Vacuum Chamber

Due to the complex flow field of ink in the vacuum chamber and the rapid diffusion of the ink, as described in Section 2.3.1, the injection of the ink into the side blow nozzle and the bottom blow nozzle with a syringe is performed, respectively. After adding the ink, a photo was taken at every 0.4 s, and a total of six photos were taken to visualize the flow of ink within 2 s after entering the vacuum chamber. The photos of different schemes under the tracer injection at the sidewall nozzle conditions are shown in Figure 7. It is important to note that the ink is injected at a 45-degree angle on the sidewall of the vacuum chamber. It diffuses from the up-snorkel to the down-snorkel.

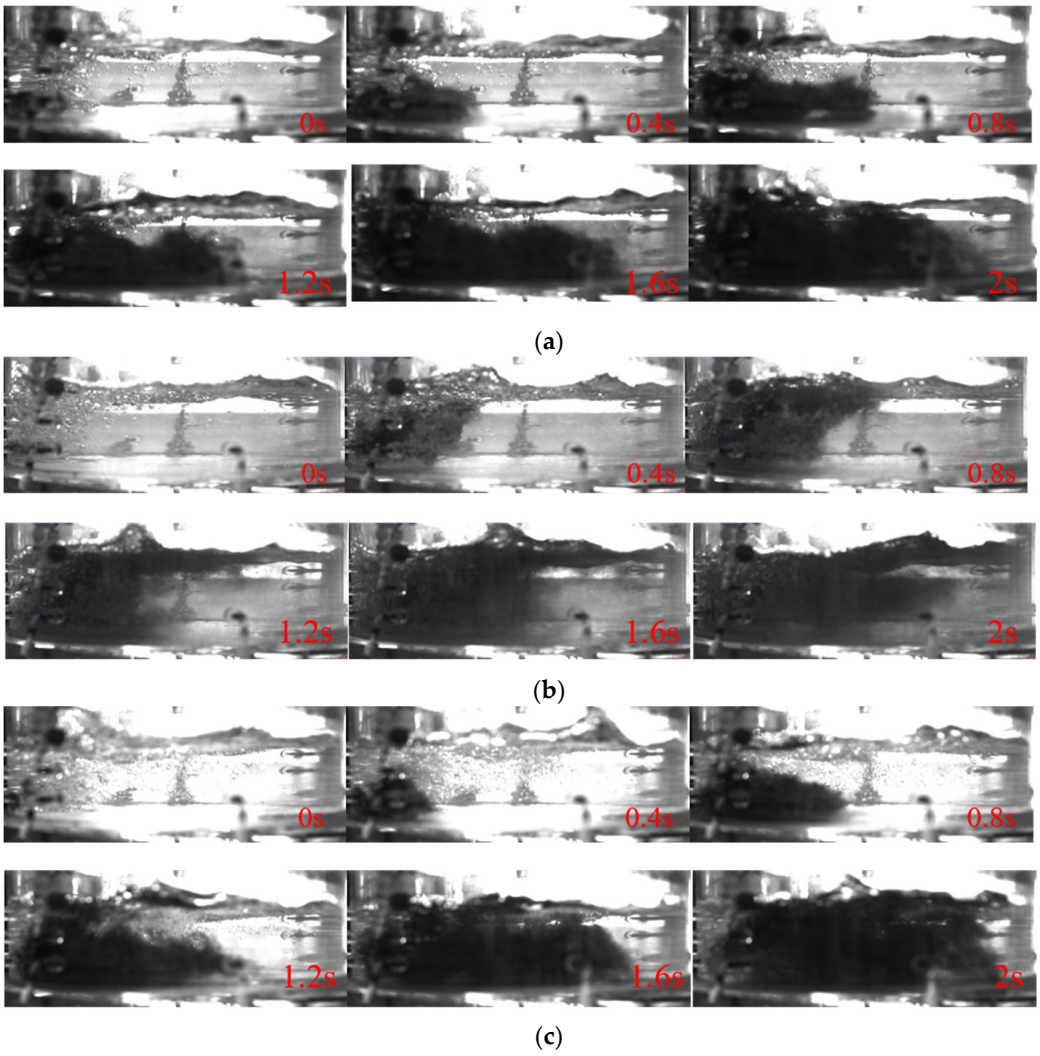


Figure 7. Photos of the sidewall injection of ink at (**a**) 25 L/min, (**b**) 25 + side-blowing 20 L/min, and (**c**) 45 L/min.

A further schematic diagram is plotted in Figure 8. For the results in Figure 8a, the ink continues to spread outward and ultimately exits the vacuum chamber through the down-snorkel. As shown in Figure 8b, following the ink injection, side-blowing significantly enhances the upward dispersion of the ink while suppressing its downward movement. This interaction results in a triangular-shaped flow pattern, as the gas introduced from the sidewall induces a diagonally upward motion of the ink. Consequently, the ink migrates toward the down-snorkel and exits the vacuum chamber into the ladle. Figure 8c demonstrates that injecting ink at a 45-degree angle on the chamber's side with an increased gas

flow rate (case 2) leads to a rise in fluid velocity and a marked acceleration of ink diffusion. Compared to a gas flow rate of 25 L/min, the ink moves more rapidly from the sidewall to the down-snorkel, and the diffusion area is reduced. This reduction indicates a shorter residence time of the ink within the vacuum chamber.

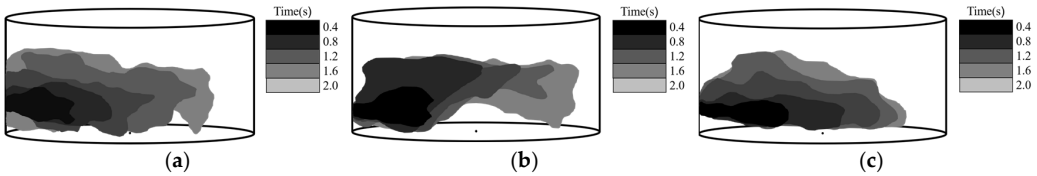


Figure 8. Visualizations of the ink diffusion in the vacuum chamber after side-blowing, as follows: (**a**) 25 L/min, (**b**) 25 + side-blowing 20 L/min, and (**c**) 45 L/min.

3.1.3. Flow Visualization After the Injection of Ink from the Nozzle at the Bottom of the Vacuum Chamber

The photos of different schemes under the tracer injection at the bottom wall nozzle of the vacuum chamber conditions are shown in Figure 9.

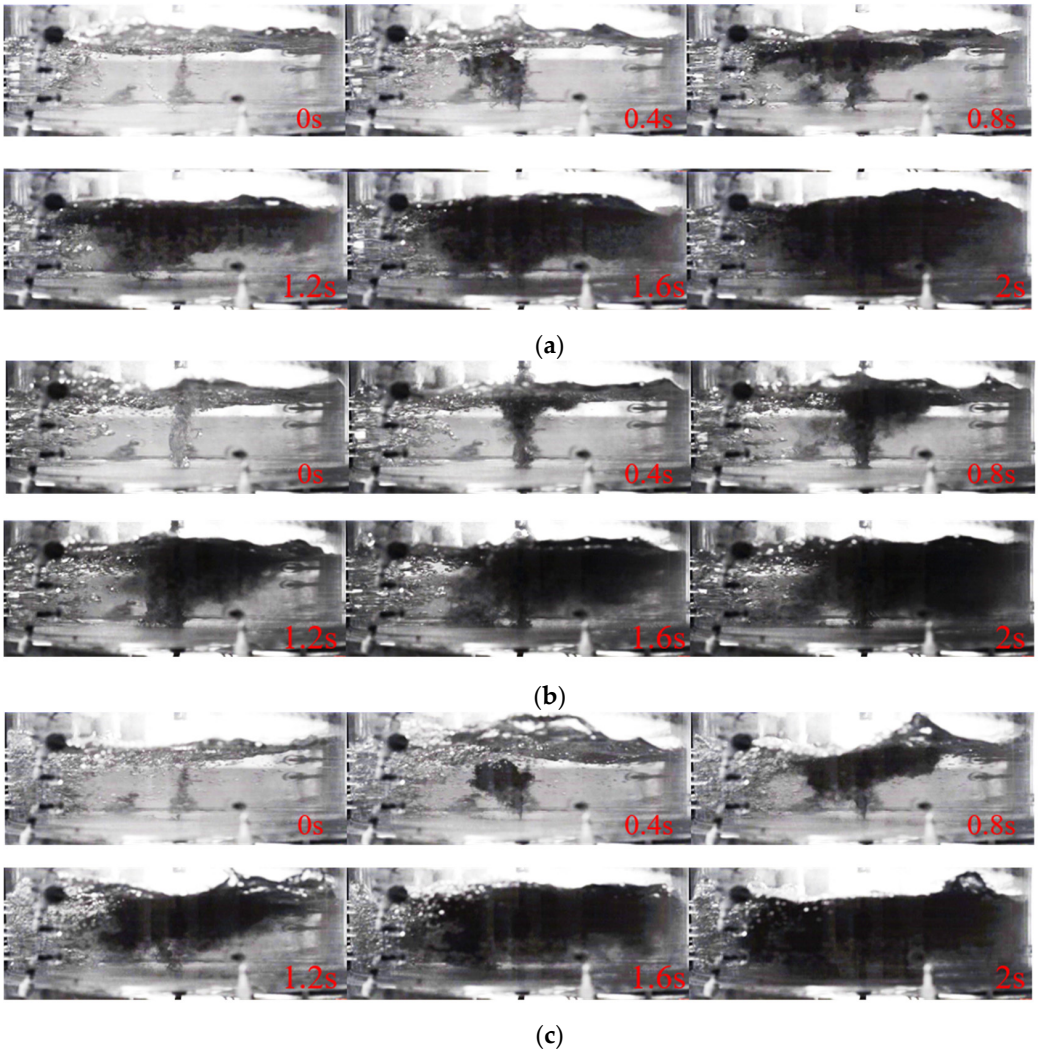


Figure 9. Photos of the bottom wall injection of ink: (**a**) 25 L/min, (**b**) 25 + bottom-blowing 20 L/min, and (**c**) 45 L/min.

A further schematic diagram is plotted in Figure 10. Figure 10a illustrates the injection of ink from the bottom of the vacuum chamber. Due to the continuous rise of bubbles in

the up-snorkel, a pressure differential is created within the vacuum chamber. Upon entry into the vacuum chamber, the ink first flows toward the up-snorkel side and then moves simultaneously upward and toward the down-snorkel side, forming a crescent-shaped flow field structure. Subsequently, the ink continues to diffuse with the flow field and flows into the ladle through the down-snorkel. As shown in Figure 10b, after implementing the bottom-blowing at the vacuum chamber and injecting ink simultaneously, it is observed that the crescent-shaped flow field structure is less pronounced compared to when gas is blown solely through the up-snorkel. With the introduction of gas from the bottom, the ink first diffuses upward to the liquid surface and then spreads toward the down-snorkel direction along the flow field. Finally, the ink exits the vacuum chamber and enters the ladle through the down-snorkel. Figure 10c demonstrates that an increase in the lifting gas flow rate accelerates the fluid velocity within the vacuum chamber, resulting in a more complex flow field structure. When the ink is injected from the bottom of the vacuum chamber, the diffusion speed of the ink significantly increases, exhibiting an irregular diffusion pattern within the vacuum chamber.

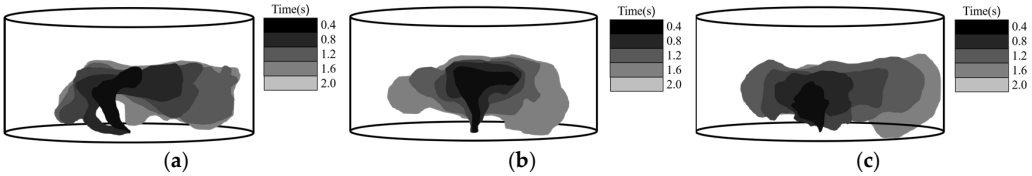


Figure 10. Visualizations of the ink diffusion in the vacuum chamber after bottom-blowing, as follows: (**a**) 25 L/min, (**b**) 25 + bottom-blowing 20 L/min, (**c**) 45 L/min.

3.2. Circulation Flow Rate

An ultrasonic flowmeter was utilized to measure the circulation flow rate. After the RH system stabilized, measurements were taken at one-second intervals. Following ten recordings, the data were averaged. Figure 11 reveals that a lifting gas flow rate of 45 L/min (case 2) results in the highest circulation flow rate, whereas a flow rate of 25 L/min (case 1) presents the lowest. Implementing either side-blowing or bottom-blowing in the vacuum chamber can increase the circulation flow rate, with side-blowing proving more effective than bottom-blowing. Additionally, a comparison of circulation flow rates shows that implementing bottom-blowing does not significantly increase this parameter. This result aligns with the visualization experiment findings.

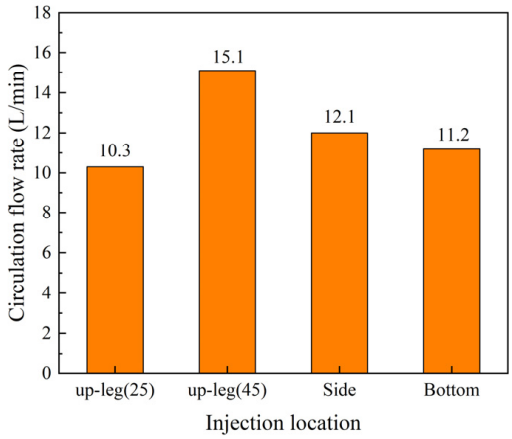


Figure 11. Circulation flow rate.

3.3. Liquid Level Fluctuation

Figure 12 illustrates the fluctuations within the vacuum chamber under four different operating conditions, captured by a high-speed camera. When the lifting gas flow rate is 25 L/min (case 1), the liquid level fluctuation of the vacuum chamber is minimal. When the lifting gas flow rate is 45 L/min (case 2), due to the increase in bubbles, spatter and fluctuation are increased. It can be seen in Figure 12b that a liquid level fluctuation always exists from the up-snorkel side to the down-snorkel side, and there is a large fluctuation at the center of the vacuum chamber. Under this working condition, there will be a great erosion on the wall of the vacuum chamber. As can be seen from Figure 12c, after side-blowing is implemented, the lifting gas bubble will deviate from the original movement path, which will reduce the fluctuation of the liquid level above the up-snorkel but strengthen the fluctuation of the liquid level in the middle of the vacuum chamber. Because the direction of side-blowing is the same as the direction of fluid movement, the fluid velocity and circulation flow rate increase after the side-blowing is increased. After implementing the bottom-blowing, as shown in Figure 12d, a gas column will be formed at the bottom center of the vacuum chamber, resulting in a large fluctuation and accompanied by splashing. However, since the fluctuation generated by this gas column will spread around, the liquid level fluctuation and fluid flow on the side of the up-snorkel will be suppressed.

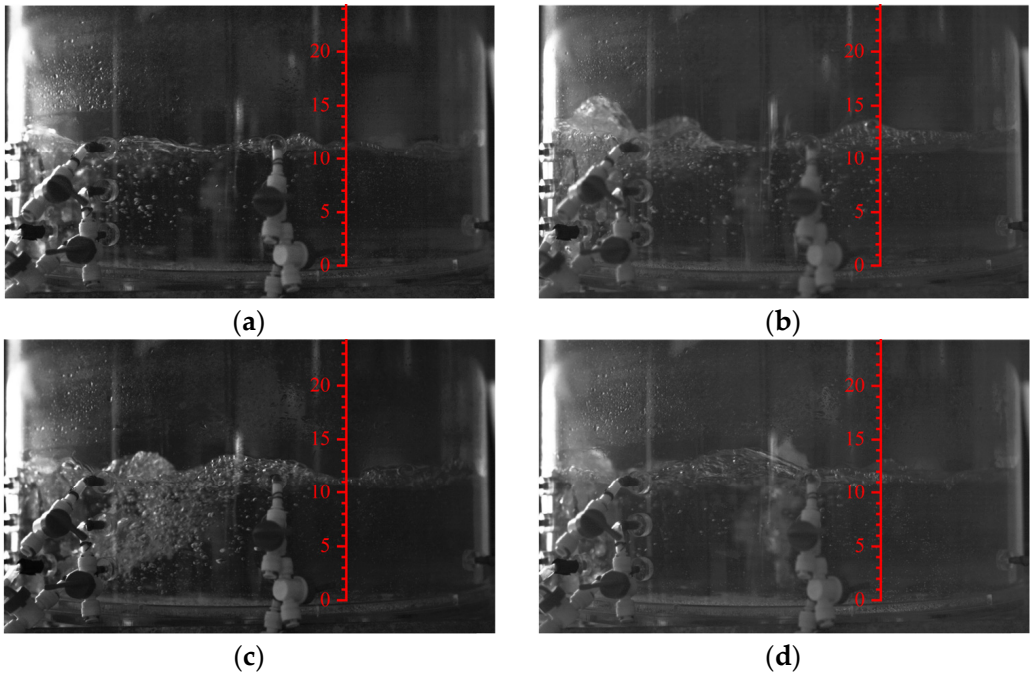


Figure 12. Liquid level fluctuation in the vacuum chamber: (**a**) 25 L/min, (**b**) 45 L/min, (**c**) side-blowing, and (**d**) bottom-blowing.

3.4. Mixing Curves

Figure 13 presents the mixing curves at monitoring points located at the bottom of the ladle under various operating conditions. As depicted in Figure 13, the conductivity curves at the ladle bottom exhibit similar trends with all four schemes. Specifically, each curve initially rises rapidly to reach a peak, then declines, undergoes a secondary response, and finally stabilizes. For all three monitoring points, the sequence of response times under the four conditions consistently follows the order that follows: 45 L/min (case 2), bottom-blowing (case 4), side-blowing (case 3), and 25 L/min (case 1). When either side-blowing or bottom-blowing are applied, their response times fall between those of 25 L/min and

45 L/min. Furthermore, the mixing curves for these combined blowing conditions are closely aligned and have similar variations.

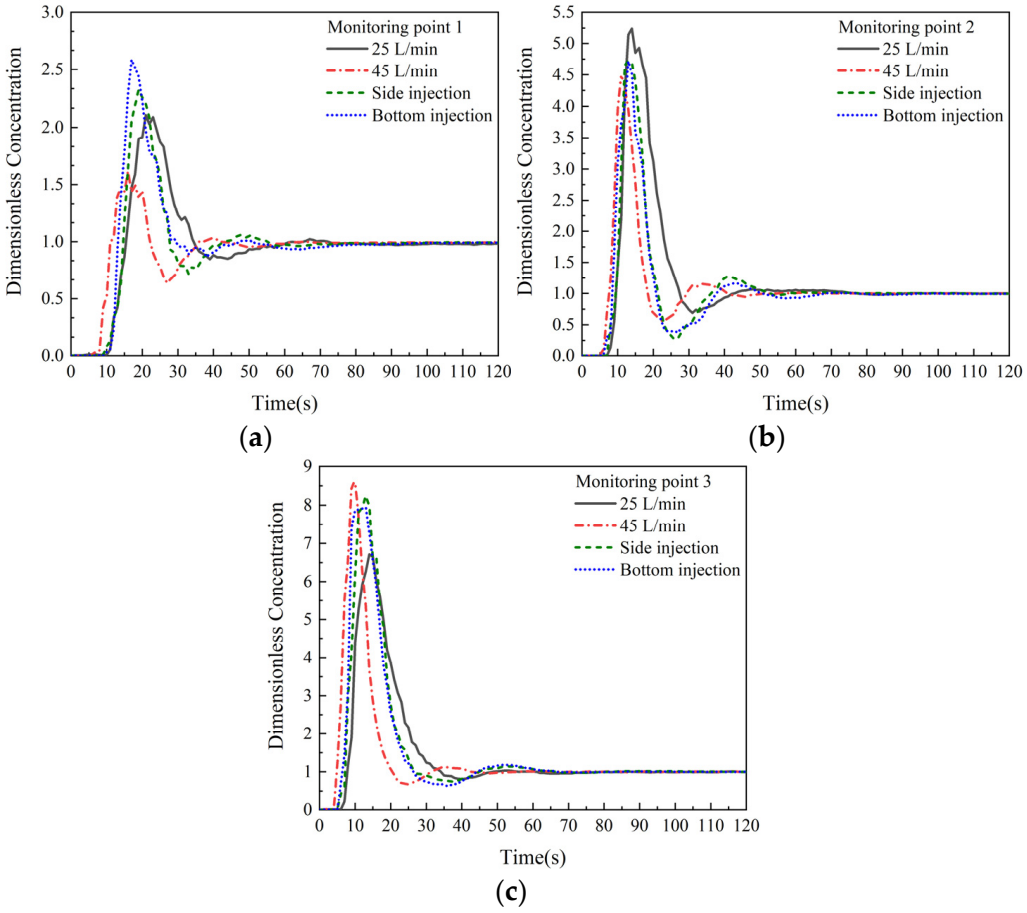


Figure 13. Mixing time curves of the monitoring points at the bottom of the ladle. (**a**) Monitoring point 1, (**b**) monitoring point 2, and (**c**) monitoring point 3.

Figure 14 presents the mixing curves at monitoring points located at the top of the ladle under four different operating schemes. For monitoring point 4, the curves under all four conditions exhibit a trend of gradually increasing from the initial response until reaching a steady mixing state (parabolic style as described in [38,81]). Although some conditions show the presence of peaks, these peaks are relatively low and decrease rapidly. This behavior can be attributed to the greater distance of this monitoring point from the down-snorkel flow stream, resulting in a weaker diffusion and mixing process. This inactive or dead zone has been reported by many research papers. As shown in Figure 14b, when the lifting gas flow rate is set to 45 L/min, the curve of monitoring point 5 responds with the fastest time. Conversely, at a gas flow rate of 25 L/min, the curve of monitoring point 5 exhibits the slowest response time. This is due to the increased circulation flow rate of case 2. However, the implementation of side-blowing and bottom-blowing does not significantly affect the mixing curves at monitoring point 5. For monitoring point 6, the mixing curves under all four schemes initially rise to higher peaks before declining to reach a steady mixing state (sinusoidal style as described in [38,81]). Since monitoring point 6 is located closer to the down-snorkel, the response time is earlier than that of point 4, indicating a more robust diffusion and mixing process of the tracer at this location.

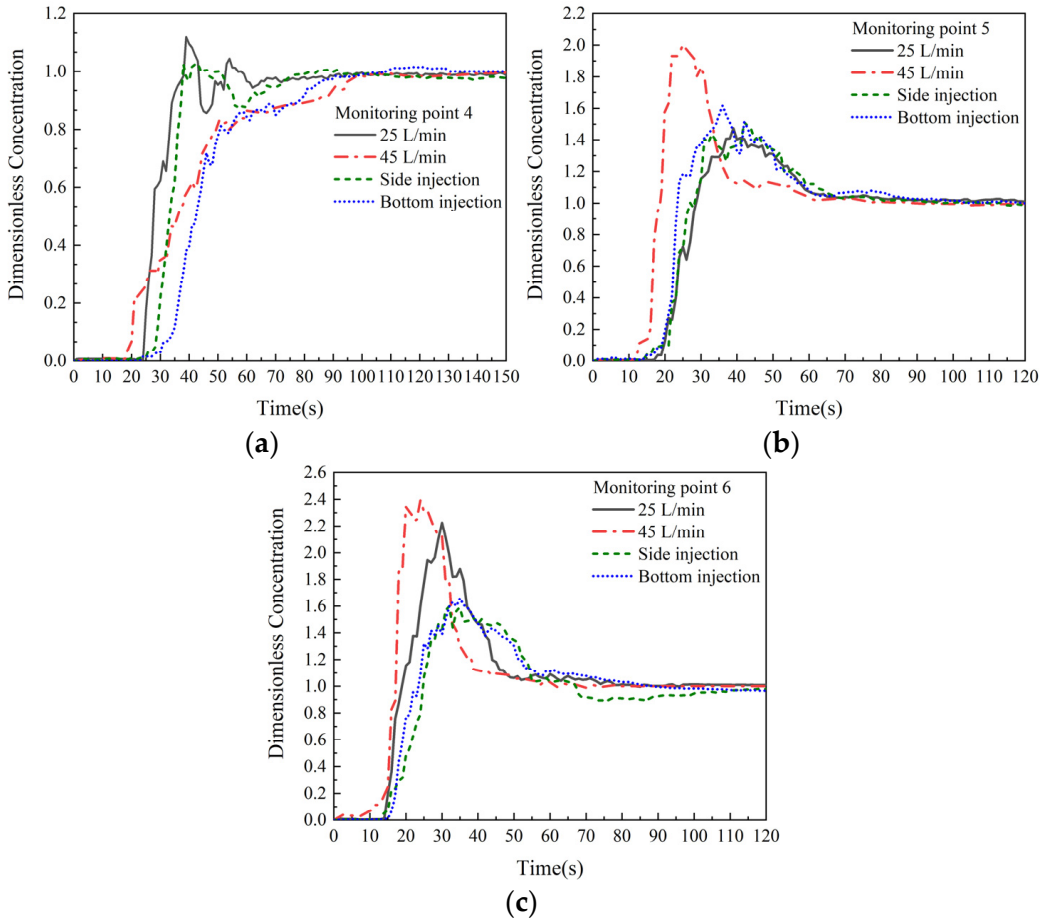


Figure 14. Mixing time curves of the monitoring points at the top of the ladle. (**a**) Monitoring point 4, (**b**) monitoring point 5, and (**c**) monitoring point 6.

Monitoring points 4, 5, and 6 are all located at the top of the ladle, situated within the dead zone of the mixing process. The effects of different operating conditions on the mixing curve of three points are distinguishable but not particularly significant.

Figure 15 presents the mixing curves at monitoring points located at the up-snorkel under four different operating schemes. As shown in the figure, the overall trend among all four schemes is similar. Specifically, each mixing curve initially rises to a peak, then declines, undergoes several fluctuations, and finally reaches a steady mixing state. When the gas flow rate is set to 45 L/min (case 2), the response time at all the three monitoring points is the earliest. The mixing curves for the other three conditions are closely aligned, exhibiting no significant differences.

Figure 16 presents the mixing curves at monitoring points located at the down-snorkel under four different operating conditions. As illustrated in the figure, the response times of all four schemes are very similar, and the overall trends exhibit minimal variation. Specifically, under the gas flow rate of 25 L/min (case 1), the peak values at all three monitoring points are higher than those observed under the other three conditions. This indicates that, under this condition, a greater volume of the tracer is entrained when the fluid flows from the down-snorkel into the ladle, resulting in a relatively weaker mixing process within the vacuum chamber.

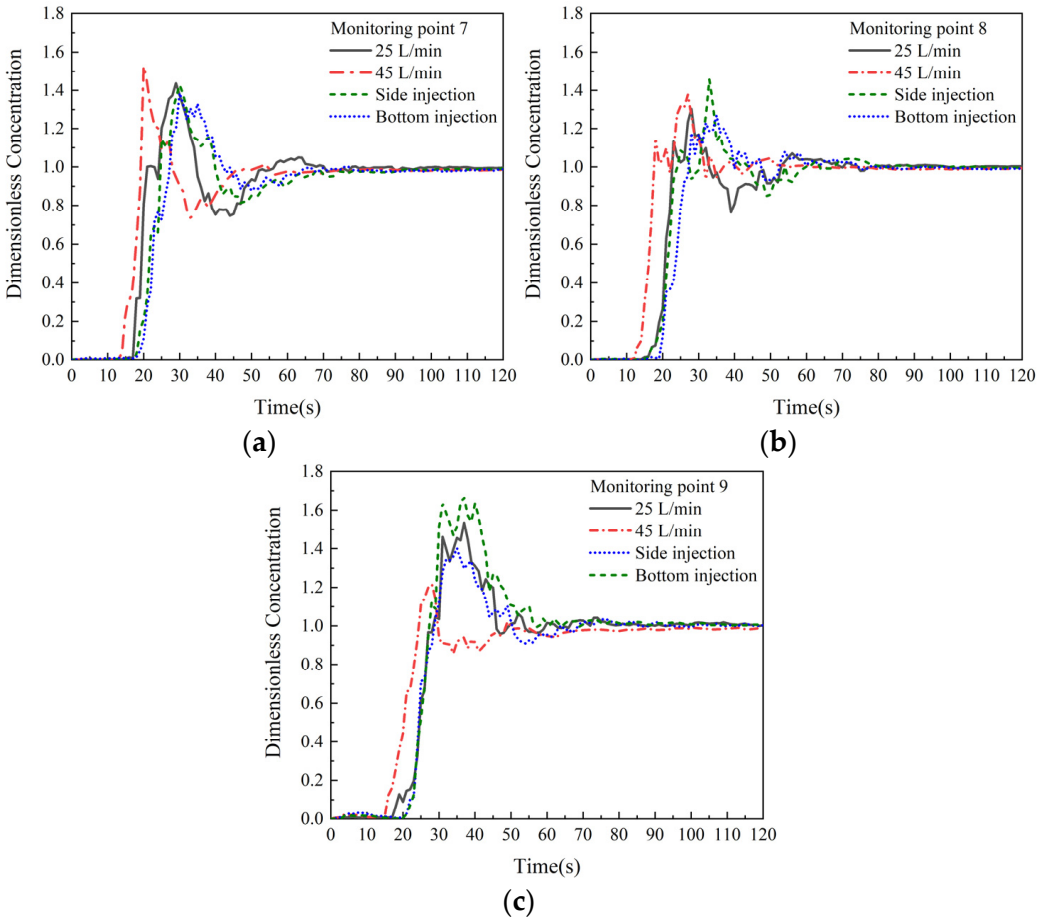


Figure 15. Mixing time curves of the monitoring points at the up-snorkel. (**a**) Monitoring point 7, (**b**) monitoring point 8, and (**c**) monitoring point 9.

Figure 17 displays the mixing times at various monitoring points under four different operating conditions. The figure indicates that the mixing times are generally lower for the conditions involving 45 L/min (case 2) and side-blowing (case 3), while the case 2 scheme exhibits the fastest circulation flow rate. As the operating conditions vary, the mixing times at the top and bottom of the ladle are more significantly affected, whereas those located around the up-snorkel and down-snorkel are less influenced. Increasing the lifting gas flow rate from 25 to 45 L/min can effectively reduce the mixing time at the bottom of the ladle, while the implementation of side-blowing efficiently decreases the mixing time at the down-snorkel. Additionally, the mixing time within the ladle is dependent on the position of the monitoring points. The implementation of side-blowing and bottom-blowing can shorten the mixing time to a certain extent, with the effect of implementing side-blowing being more pronounced than that of implementing bottom-blowing. However, the effectiveness of side-blowing and bottom-blowing is inferior to that of a gas flow rate of 45 L/min (case 2). Qi et al. [82] have demonstrated that the area near the down-snorkel was a dead zone. Monitoring points 10, 11, and 12 are located at the dead zone. Therefore, under the four working conditions, the mixing times of these points are similar and minimally affected by changes in the gas flow rate.

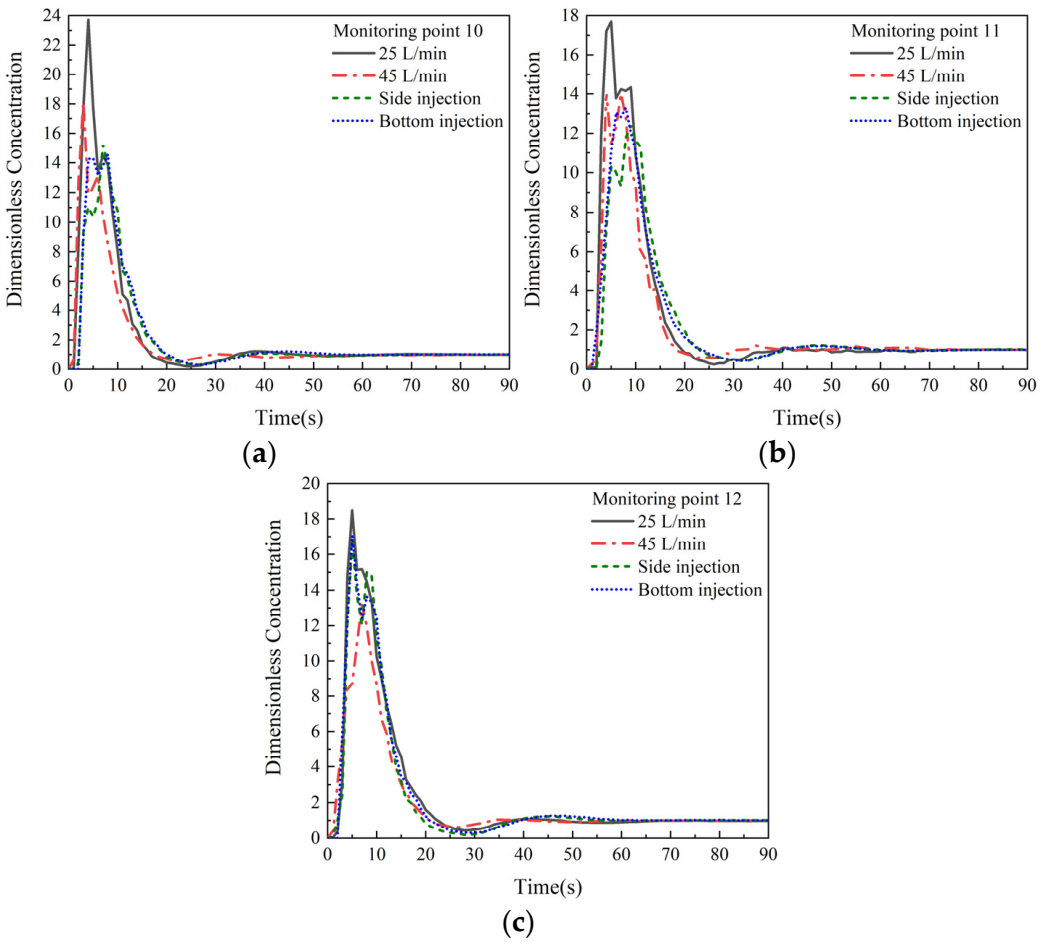


Figure 16. Mixing time curves of the monitoring points at the down-snorkel. (**a**) Monitoring point 10, (**b**) monitoring point 11, and (**c**) monitoring point 12.

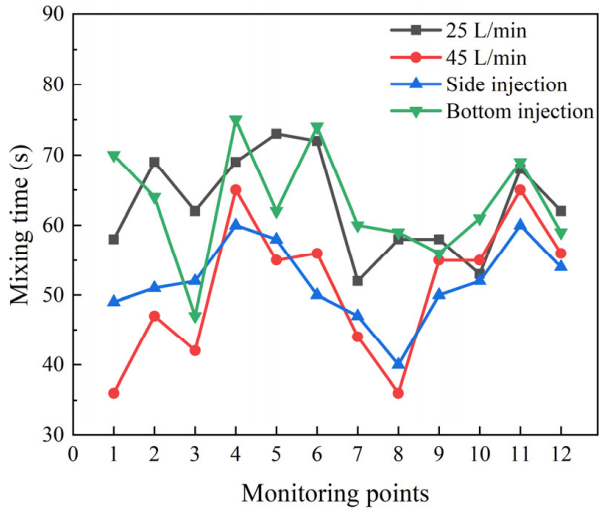


Figure 17. The mixing time at the monitoring points.

4. Conclusions

Based on the investigation of the combined blowing process involving gas blowing at the side or bottom of the vacuum chamber with up-snorkel nozzles, the following conclusions can be drawn as follows:

1. For the flow and tracer dispersion in the normal RH unit, after the ink tracer flows out from the down-snorkel, it primarily diffuses in two directions. Most of the ink flows leftward along the bottom of the ladle and continuously moves upward throughout the entire ladle, while a smaller portion adheres to the right wall of the ladle, this portion of tracer slowly ascending and diffusing. Implementing side-blowing on the sidewalls of the vacuum chamber can accelerate the diffusion rate of the ink, whereas implementing bottom-blowing in the vacuum chamber has little effect on the diffusion rate.
2. After implementing side-blowing in the RH vacuum chamber, the ink tracer is influenced by the side-blowing airflow, forming a triangular flow pattern inside the vacuum chamber. This flow pattern allows the ink tracer to spread over a greater distance within the chamber, enhancing its diffusion. After implementing bottom-blowing in the RH vacuum chamber, the crescent-shaped flow pattern of the ink tracer is weakened, and the ink tracer rises with the gas column to the liquid surface, then diffuses outward in all directions.
3. The novel blowing method enhances the operational efficiency of the RH device, significantly increasing the circulation flow rate by implementing side-blowing and bottom-blowing in the vacuum chamber. Compared with the condition of only up-snorkel blowing at 25 L/min, the implementing of side-blowing and bottom-blowing with a gas flow rate of 20 L/min resulted in circulation flow rates increasing from 10.3 m^3/h to 12.1 m^3/h and 11.2 m^3/h, respectively.
4. When the lifting gas flow rate is 45 L/min, splashing and fluctuations are more severe. After implementing the side-blowing, the lifting gas bubbles deviate from their original trajectories, resulting in reduced liquid level fluctuations above the up-snorkel but enhanced liquid level fluctuations in the middle region of the vacuum chamber. Overall, the fluctuations are reduced after implementing the side-blowing. After implementing the bottom-blowing, a gas column forms at the center region of the vacuum chamber bottom, resulting in splashing. However, the fluctuations generated by this gas column suppress the fluctuations at the up-snorkel region.
5. Increasing the lifting gas flow rate and implementing side-blowing can significantly reduce the mixing time at the top and bottom of the ladle. At monitoring points near the down-snorkel, it was observed that when the lifting gas flow rate is 25 L/min, the homogenization within the vacuum chamber is the worst, with the highest tracer concentration coming from the down-snorkel. Monitoring points at the down-snorkel outlet are obstructed by the snorkels, and the mixing times at these points vary minimally with operating conditions. After implementing bottom-blowing, the mixing times at monitoring points 3 and 5 significantly decreased, while the mixing times at the remaining monitoring points showed little difference compared to the condition with a 25 L/min lifting gas flow rate. Overall, the improvement effect of bottom-blowing on the mixing time is not obvious.
6. Based on this study, implementing side-blowing to the RH vacuum chamber has more advantages than implementing bottom-blowing. Adding side-blowing can not only alleviate splashing but also increase the mixing rate, which shows great industrial prospects. Further studies are required to optimize the position, height, and number of nozzles as well as the gas flow rate of the side-blowing, with the aid of water models, CFD simulations, and industrial experiments.

Author Contributions: Conceptualization, C.C. and L.X.; methodology, C.C. and L.X.; software, Y.Z., J.W., H.W. and Z.X.; validation, Z.M., Z.X., J.W., Y.Z. and R.X.; formal analysis, L.X., H.W. and Y.Z.; investigation, L.X., Y.Z., J.W., H.W., Z.M., R.X. and Z.X.; resources, C.C., W.L. and X.N.; data curation, L.X., Y.Z., H.W., Z.X. and J.W.; writing—original draft preparation, L.X., Y.Z., J.W. and H.W.; writing—review and editing, C.C., W.L. and X.N.; visualization, Y.Z., H.W., Z.M. and R.X.; supervision, X.N., W.L. and C.C.; project administration, C.C.; funding acquisition, J.W. and C.C. All authors have read and agreed to the published version of the manuscript.

Funding: This research was funded by the research project 'Mechanism of Combined Blowing and Alloy Homogenization in RH Vacuum Refining of Silicon Steel for New Energy Vehicles', which is supported by the "Applied Fundamental Research Programs of Shanxi Province, grant number 202403021222046" and the Graduate Innovation Project of Shanxi Province, grant number 2024KY277.

Data Availability Statement: The original contributions presented in this study are included in the article. Further inquiries can be directed to the corresponding author.

Acknowledgments: Those who have participated in the experiments are sincerely acknowledged. They are Xin Ouyang, Ruijie Ren, Mingming Yang, Ruiyun Cao, Huibo Yang, Tianyang Wang, Shiwei Su, and Yunzhe Zhang. The comments from reviewers are sincerely acknowledged.

Conflicts of Interest: Authors Liqiang Xue and Zhibo Xu were partially employed by the company Shanxi Taigang Stainless Steel Co., Ltd. The remaining authors declare that the research was conducted in the absence of any commercial or financial relationships that could be construed as potential conflicts of interest.

References

1. Oda, Y.; Kohno, M.; Honda, A. Recent development of non-oriented electrical steel sheet for automobile electrical devices. *J. Magn. Magn. Mater.* **2008**, *320*, 2430–2435. [CrossRef]
2. Cheng, C.Y.; Zhong, B.L.; Ni, Z.X.; Jing, W.Q.; Zhang, S.Q.; Liu, J. Research progress on the control of force and magnetic properties of high-strength non-oriented silicon steel for driving motors of new energy vehicles. *J. Eng. Sci.* **2023**, *45*, 1482–1492.
3. Guo, F.; Niu, Y.; Fu, B.; Qiao, J.; Qiu, S. Influence Mechanisms of Cold Rolling Reduction Rate on Microstructure, Texture and Magnetic Properties of Non-Oriented Silicon Steel. *Crystals* **2024**, *14*, 853. [CrossRef]
4. Shao, K.; Niu, Y.; Pei, Y.; Qiao, J.; Pan, H.; Wang, H. Effects of Continuous Rolling and Reversible Rolling on 2.4% Si Non-Oriented Silicon Steel. *Crystals* **2024**, *14*, 824. [CrossRef]
5. Liu, X.J.; Yang, J.C.; Ren, H.P.; Jia, X.B.; Zhang, M.Y.; Yang, C.Q. Effect of solute Ce, Mn, and Si on mechanical properties of silicon steel: Insights from DFT calculations. *J. Iron Steel Res. Int.* **2024**, *31*, 700–709. [CrossRef]
6. Pindar, S.; Pande, M.M. Assessment of Si-O Equilibria and Nonmetallic Inclusion Characteristics in High Silicon Steels. *Steel Res. Int.* **2023**, *94*, 2300115. [CrossRef]
7. Pindar, S.; Pande, M.M. Investigation of Inclusion Characteristics in Ferrosilicon Killed High Silicon Steels. *Steel Res. Int.* **2024**, *95*, 2400331. [CrossRef]
8. Ren, Q.; Hu, Z.Y.; Liu, Y.X.; Zhang, W.C.; Gao, Z.Q.; Zhang, L.F. Effect of lanthanum on inclusions in non-oriented electrical steel slabs. *J. Iron Steel Res. Int.* **2024**, *31*, 1680–1691. [CrossRef]
9. Cao, J.Q.; Chen, C.; Xue, L.Q.; Li, Z.; Zhao, J.; Lin, W.M. Analysis of the inclusions in the whole smelting process of non-oriented silicon steel DG47A. *Iron Steel* **2023**, *58*, 61–71. [CrossRef]
10. Wang, T.; Chen, C.; Mu, W.Z.; Xue, L.Q.; Cao, J.Q.; Lin, W.M. Analysis of inclusions in whole smelting process of non-oriented silicon steel 23W1700 by rare earth treatment. *Iron Steel* **2024**, *59*, 92–103. [CrossRef]
11. Wang, H.; Niu, Y.; Ling, H.; Qiao, J.; Zhang, Y.; Zhong, W.; Qiu, S. Modification of Rare Earth Ce on Inclusions in W350 Non-Oriented Silicon Steel. *Metals* **2023**, *13*, 453. [CrossRef]
12. Wang, H.; Niu, Y.; Ling, H.; Qiao, J.; Zhang, Y.; Zhong, W.; Qiu, S. Effects of Rare Earth La–Ce Alloying Treatment on Modification of Inclusions and Magnetic Properties of W350 Non-Oriented Silicon Steel. *Metals* **2023**, *13*, 626. [CrossRef]
13. Kato, Y.; Nakato, H.; Fujii, T.; Ohmiya, S.; Takatori, S. Fluid flow in ladle and its effect on decarburization rate in RH degasser. *ISIJ Int.* **1993**, *33*, 1088–1094. [CrossRef]
14. Ling, H.T.; Zhang, L.F. Investigation on the Fluid Flow and Decarburization Process in the RH Process. *Metall. Mater. Trans. B* **2018**, *49B*, 2709–2721. [CrossRef]
15. Liu, C.; Zhang, L.F.; Sun, Y.; Yang, W. Large Eddy Simulation on the Transient Decarburization of the Molten Steel During RH Refining Process. *Metall. Mater. Trans. B* **2022**, *53*, 670–681. [CrossRef]

16. Peng, K.Y.; Liu, C.; Zhang, L.F.; Sun, Y. Numerical Simulation of Decarburization Reaction with Oxygen Blowing During RH Refining Process. *Metall. Mater. Trans. B* **2022**, *53*, 2004–2017. [CrossRef]
17. Chen, S.F.; Lei, H.; Wang, M.; Yang, B.; Dou, W.X.; Chang, L.S.; Zhang, H.W. Ar-CO-liquid Steel Flow with Decarburization Chemical Reaction in Single Snorkel Refining Furnace. *Int. J. Heat Mass Transfer.* **2020**, *146*, 118857. [CrossRef]
18. Dong, W.L.; Xu, A.J.; Liu, B.S.; Zhou, H.C.; Ji, C.X.; Wang, S.J.; Li, H.B.; Wang, T.H. Mechanism and Model of Nitrogen Absorption of Molten Steel During N_2 Injection Process in RH Vacuum. *Metall. Mater. Trans. B* **2024**, *55*, 72–82. [CrossRef]
19. Wei, J.H.; Jiang, X.Y.; Wen, L.J.; Li, B. Mass Transfer Characteristics between Molten Steel and Particles under Conditions of RH-PB(IJ) Refining Process. *ISIJ Int.* **2007**, *47*, 408–417. [CrossRef]
20. Feng, K.; Liu, A.; Dai, K.; Feng, S.; Ma, J.; Xie, J.; Wang, B.; Yu, Y.; Zhang, J. Effect of gas rate and position of powder injection on RH refining process using numerical simulation. *Powder Technol.* **2017**, *314*, 649–659. [CrossRef]
21. Liu, Z.; Lou, W.T.; Zhu, M.Y. Powder transport behavior in RH degasser with powder injection through up snorkel: A transient numerical model. *J. Iron Steel Res. Int.* **2023**, *30*, 1156–1170. [CrossRef]
22. Liu, Z.; Lou, W.; Zhu, M.Y. Numerical Analysis of Fluid Flow and Powder Transport Characteristics of RH-Degasser Ladle Bottom Powder Injection (RH-PBI) Process. *Metall. Mater. Trans. B* **2024**, *55*, 418–430. [CrossRef]
23. Peng, K.Y.; Sun, Y.; Peng, X.X.; Chen, W.; Zhang, L.F. Numerical Simulation on the Desulfurization of the Molten Steel during RH Vacuum Refining Process by CaO Powder Injection. *Metall. Mater. Trans. B* **2023**, *54*, 438–449. [CrossRef]
24. Silva, A.M.B.; Peixoto, J.J.M.; da Silva, C.A. Numerical and Physical Modeling of Steel Desulfurization on a Modified RH Degasser. *Metall. Mater. Trans. B* **2023**, *54*, 2651–2669. [CrossRef]
25. Zhang, L.F.; Peng, K.Y.; Ren, Y. Kinetic Analysis for Steel Desulfurization during Ruhrstahl–Heraeus Process. *Steel Res. Int.* **2023**, *95*, 2300399. [CrossRef]
26. She, C.J.; Peng, K.Y.; Sun, Y.; Ren, Y.; Zhang, L.F. Kinetic Model of Desulfurization During RH Refining Process. *Metall. Mater. Trans. B* **2024**, *55*, 92–104. [CrossRef]
27. Liu, C.; Duan, H.; Zhang, L. Modeling of the Melting of Aluminum Particles during the RH Refining Process. *Metals* **2019**, *9*, 442. [CrossRef]
28. Wang, H.J.; Xu, R.; Ling, H.T.; Zhong, W.; Chang, L.Z.; Qiu, S.T. Numerical simulation of fluid flow and alloy melting in RH process for electrical steels. *J. Iron Steel Res. Int.* **2022**, *29*, 1423–1433. [CrossRef]
29. Liu, C.; Peng, K.Y.; Wang, Q.; Li, G.Q.; Wang, J.J.; Zhang, L.F. CFD Investigation of Melting Behaviors of Two Alloy Particles During Multiphase Vacuum Refining Process. *Metall. Mater. Trans. B* **2023**, *54*, 2174–2187. [CrossRef]
30. Chen, S.F.; Lei, H.; Hou, H.C.; Ding, C.Y.; Zhang, H.; Zhao, Y. Collision-coalescence Among Inclusions with Bubble Attachment and Transport in Molten Steel of RH. *J. Mater. Res. Technol.* **2021**, *15*, 5141–5150. [CrossRef]
31. Kim, T.S.; Yang, J.; Park, J.H. Effect of Physicochemical Properties of Slag on the Removal Rate of Alumina Inclusions in the Ruhrstahl–Heraeus (RH) Refining Conditions. *Metall. Mater. Trans. B* **2022**, *53*, 2523–2533. [CrossRef]
32. Peng, K.Y.; Wang, J.J.; Li, Q.L.; Liu, C.; Zhang, L.F. Multiphase Simulation on the Collision, Transport, and Removal of Non-metallic Inclusions in the Molten Steel During RH Refining. *Metall. Mater. Trans. B* **2023**, *54*, 928–943. [CrossRef]
33. Sun, Y.; Duan, H.; Zhang, L. A boundary layer model for capture of inclusions by steel–slag interface in a turbulent flow. *J. Iron Steel Res. Int.* **2023**, *30*, 1101–1108. [CrossRef]
34. Cao, J.Q.; Li, Y.; Lin, W.M.; Che, J.L.; Zhou, F.; Tan, Y.F.; Li, D.L.; Dang, J.; Chen, C. Assessment of Inclusion Removal Ability in Refining Slags Containing Ce_2O_3. *Crystals* **2023**, *13*, 202. [CrossRef]
35. Ling, H.T.; Li, F.; Zhang, L.F.; Conejo, A.N. Investigation on the Effect of Nozzle Number on the Recirculation Rate and Mixing Time in the RH Process Using VOF+DPM Model. *Metall. Mater. Trans. B* **2016**, *47*, 1950–1961. [CrossRef]
36. Zhu, B.H.; Liu, Q.C.; Zhao, D.; Ren, S.; Xu, M.R.; Yang, B.C.; Hu, B. Effect of Nozzle Blockage on Circulation Flow Rate in Up-Snorkel during the RH Degasser Process. *Steel Res. Int.* **2016**, *87*, 136–145. [CrossRef]
37. Li, L.; Chen, C.; Tao, X.; Qi, H.; Liu, T.; Yan, Q.; Deng, F.; Allayev, A.; Lin, W.; Wang, J. Effect of Salt Solution Tracer Dosage on the Transport and Mixing of Tracer in a Water Model of Asymmetrical Gas-Stirred Ladle with a Moderate Gas Flowrate. *Symmetry* **2024**, *16*, 619. [CrossRef]
38. Tao, X.; Qi, H.; Guo, Z.; Wang, J.; Wang, X.; Yang, J.; Zhao, Q.; Lin, W.; Yang, K.; Chen, C. Assessment of Measured Mixing Time in a Water Model of Eccentric Gas-Stirred Ladle with a Low Gas Flow Rate: Tendency of Salt Solution Tracer Dispersions. *Symmetry* **2024**, *16*, 1241. [CrossRef]
39. Xu, Z.; Ouyang, X.; Chen, C.; Li, Y.; Wang, T.; Ren, R.; Yang, M.; Zhao, Y.; Xue, L.; Wang, J. Numerical Simulation of the Density Effect on the Macroscopic Transport Process of Tracer in the Ruhrstahl–Heraeus (RH) Vacuum Degasser. *Sustainability* **2024**, *16*, 3923. [CrossRef]
40. Cwudziński, A.; Falkus, J.; Podolska-Loska, A. Numerical, Physical, and Industrial Investigations on Hot Metal Desulphurization—From Macromixing Conditions to Reaction Rate Phenomena. *Materials* **2024**, *17*, 5858. [CrossRef]
41. Zhao, Z.J.; Wang, M.; Song, L.; Bao, Y.P. Splashing Simulation of Liquid Steel Drops during the Ruhrstahl Heraeus Vacuum Process. *Metals* **2020**, *10*, 1070. [CrossRef]

42. Liu, J.G.; Xie, J.Y.; Shi, Z.Q.; Li, Z.J.; Chu, R.S.; Hao, N. Numerical Simulation of Removal of Cold Steel in Inner Wall of Vacuum Chamber of 100 t RH Unit by Top Oxygen-Lance Blowing and Application. *Spec. Steel* **2018**, *39*, 1–5. [CrossRef]
43. Katoh, T.; Okamoto, T. Mixing of Molten Steel in a Ladle with RH Reactor by the Water Model Experiment. *Denki Seiko* **1979**, *50*, 128–137. [CrossRef]
44. Wei, J.H.; Yu, N.W.; Fan, Y.Y.; Yang, S.L.; Ma, J.C.; Zhu, D.P. Study on Flow and Mixing Characteristics of Molten Steel in RH and RH-KTB Refining Processes. *J. Shanghai Univ.* **2002**, *2*, 167–175. [CrossRef]
45. Silva, C.A.D.; Silva, I.A.D.; Martins, E.M.D.C.; Seshadri, V.; Perim, C.A.; Filho, G.A.V. Fluid Flow and Mixing Characteristics in RH Degasser of Companhia Siderúrgica de Tubarão, and Influence of Bottom Gas Injection and Nozzle Blockage through Physical Modelling Study. *Ironmak. Steelmak.* **2004**, *31*, 37–42. [CrossRef]
46. Seshadri, V.; Silva, C.A.; Silva, I.A.; Vargas, G.A.; Lascosqui, P.S.B. Decarburisation Rates in RH–KTB Degasser of CST Steel Plant through Physical Modelling Study. *Ironmak. Steelmak.* **2006**, *33*, 34–38. [CrossRef]
47. Zhang, L.F.; Li, F. Investigation on the Fluid Flow and Mixing Phenomena in a Ruhrstahl-Heraeus (RH) Steel Degasser Using Physical Modeling. *JOM* **2014**, *66*, 1227–1240. [CrossRef]
48. Yoshitomi, K.; Nagase, M.; Uddin, M.A.; Kato, Y. Fluid Mixing in Ladle of RH Degasser Induced by Down Flow. *ISIJ Int.* **2016**, *56*, 1119–1123. [CrossRef]
49. Mukherjee, D.; Shukla, A.K.; Senk, D.G. Cold Model-Based Investigations to Study the Effects of Operational and Nonoperational Parameters on the Ruhrstahl-Heraeus Degassing Process. *Metall. Mater. Trans. B* **2017**, *48*, 763–771. [CrossRef]
50. Liu, C.; Zhang, L.F.; Li, F.; Peng, K.Y.; Liu, F.G.; Liu, Z.T.; Zhao, Y.Y.; Yang, W.; Zhang, J. Water Modeling on Circulating Flow and Mixing Time in a Ruhrstahl–Heraeus Vacuum Degasser. *Steel Res. Int.* **2021**, *92*, 2000608. [CrossRef]
51. Xing, L.D.; Xiao, W.; Zhang, Z.F.; Bao, Y.P.; Wang, M. Physical Modeling Study for Process Optimization of 300-ton RH Vacuum Refining Furnace. *J. Sustain. Metall.* **2024**, *10*, 386–396. [CrossRef]
52. Shirabe, K.; Szekely, J. A Mathematical Model of Fluid Flow and Inclusion Coalescence in the RH vacuum Degassing System. *Trans. Iron Steel Inst. Jpn.* **1983**, *23*, 465–474. [CrossRef]
53. Geng, D.Q.; Lei, H.; He, J.C. Numerical Simulation of the Multiphase Flow in the Rheinsahl–Heraeus (RH) System. *Metall. Mater. Trans. B* **2010**, *41B*, 234–247. [CrossRef]
54. Chen, G.J.; Wang, Q.Q.; He, S.P. Computational Fluid Dynamics Modeling of Argon-Steel (-Slag) Multiphase Flow in an Ruhrstahl-Heraeus Degasser: A Review of Past Numerical Studies. *Steel Res. Int.* **2023**, *94*, 2200298. [CrossRef]
55. Xin, Z.; Zhang, J.; Peng, K.; Zhang, J.; Zhang, C.; Liu, Q. Modeling of LF refining process: A review. *J. Iron Steel Res. Int.* **2024**, *31*, 289–317. [CrossRef]
56. Khan, S.; Idrees, M.; Mushtaq, M.U.; Hussain, S. Two Dimensional (2D) Multi-Scale Modeling of Fixed Bed Adsorption Column Using Computational Fluid Dynamics (CFD) Simulation. *Arch. Adv. Eng. Sci.* **2024**, *2*, 1–9. [CrossRef]
57. Chen, G.J.; He, S.P. Volume of fluid simulation of single argon bubble dynamics in liquid steel under RH vacuum conditions. *J. Iron Steel Res. Int.* **2024**, *31*, 828–837. [CrossRef]
58. Li, H.; Liu, J.X.; Ren, Q.; Zhang, L.F. Effect of Ruhrstahl Heraeus Refining Time on Inclusions and Rolling Contact Fatigue Life of a High-Carbon Chromium Bearing Steel. *Steel Res. Int.* **2023**, *94*, 2200977. [CrossRef]
59. Ouyang, X.; Lin, W.M.; Luo, Y.Z.; Zhang, Y.X.; Fan, J.P.; Chen, C.; Cheng, G.G. Effect of Salt Tracer Dosages on the Mixing Process in the Water Model of a Single Snorkel Refining Furnace. *Metals* **2022**, *12*, 1948. [CrossRef]
60. Luo, Y.; Liu, C.; Ren, Y.; Zhang, L.F. Modeling on the Fluid Flow and Mixing Phenomena in a RH Steel Degasser with Oval Down-Leg Snorkel. *Steel Res. Int.* **2018**, *89*, 1800048. [CrossRef]
61. Ling, H.; Zhang, L.F.; Liu, C. Effect of Snorkel Shape on the Fluid Flow during RH Degassing Process: Mathematical Modelling. *Ironmak. Steelmak.* **2018**, *45*, 145–155. [CrossRef]
62. He, Q.; Yao, T.L.; Lin, L.; Li, X.C.; Ni, B.; Li, L.F. An experimental study on RH vacuum chamber with a weir. *J. Iron Steel Res. Int.* **2023**, *30*, 1929–1938. [CrossRef]
63. Chen, C.; Cheng, G.G.; Yang, H.K.; Hou, Z.B. Physical modeling of Fluid flow Characteristics in a Delta Shaped, Four-Strand Continuous Casting Tundish with Different Flow Control Devices. *Adv. Mater. Res.* **2011**, *284-286*, 1071–1079. [CrossRef]
64. Zhao, S.; Zhu, S.; Ge, Y.; Wang, J.; Xu, D.; Li, Z.; Chen, C. Simulation of Fluid Flow and Inclusion Removal in Five-Flow T-Type Tundishes with Porous Baffle Walls. *Metals* **2023**, *13*, 215. [CrossRef]
65. Fan, J.; Li, Y.; Chen, C.; Ouyang, X.; Wang, T.; Lin, W. Effect of Uniform and Non-Uniform Increasing Casting Flow Rate on Dispersion and Outflow Percentage of Tracers in Four Strand Tundishes under Strand Blockage Conditions. *Metals* **2022**, *12*, 1016. [CrossRef]
66. Geng, D.Q.; Lei, H.; He, J.C. Simulation on flow field and mixing phenomenon in RH degasser with ladle bottom blowing. *Ironmak. Steelmak.* **2012**, *39*, 431–438. [CrossRef]
67. Dong, J.F.; Feng, C.; Zhu, R.; Wei, G.S.; Jiang, J.J.; Chen, S.Z. Simulation and Application of Ruhrstahl–Heraeus (RH) Reactor with Bottom-Blowing. *Metall. Mater. Trans. B* **2021**, *52*, 2127–2138. [CrossRef]

68. Dong, J.F.; Feng, C.; Zhu, R.; Wei, G.S.; Xia, T.; Zhang, Q.N. Analysis of fluid flow characteristics of RH reactor with different bottom-blowing arrangements. *Ironmak. Steelmak.* **2023**, *50*, 325–335. [CrossRef]
69. Wang, R.D.; Jin, Y.; Cui, H. The Flow Behavior of Molten Steel in an RH Degasser Under Different Ladle Bottom Stirring Processes. *Metall. Mater. Trans. B* **2022**, *53*, 342–351. [CrossRef]
70. Zhang, S.; Liu, J.H.; He, Y.; Zhou, C.H.; Yuan, B.H.; Mclean, A. Bubble formation by argon injection through the down-leg snorkel with Ruhrstahl-Heraeus (RH) circulating flow. *J. Mater. Process. Technol.* **2022**, *306*, 117647. [CrossRef]
71. Zhang, S.; Liu, J.H.; He, Y.; Zhou, C.H.; Yuan, B.H.; Zhang, M.; Barati, M. Study of Dispersed Micro-bubbles and Improved Inclusion Removal in Ruhrstahl–Heraeus (RH) Refining with Argon Injection Through Down Leg. *Metall. Mater. Trans. B* **2023**, *54*, 2347–2359. [CrossRef]
72. Inoue, S.; Furuno, Y.; Usui, T.; Miyahara, S. Acceleration of Decarburization in RH Vacuum Degassing Process. *ISIJ Int.* **1992**, *32*, 120–125. [CrossRef]
73. Zheng, W.; He, Z.P.; Li, G.Q.; Tu, H.; Zhang, Z. Physical Simulation of Effect of Injection Parameters on Circulation Flow Rate and Mixing Time in RH Vacuum Refining Process. *J. Iron Steel Res.* **2017**, *29*, 373–381. [CrossRef]
74. Neves, L.; Oliveira, H.; Tavares, R. Evaluation of the Effects of Gas Injection in the Vacuum Chamber of a RH Degasser on Melt Circulation and Decarburization Rates. *ISIJ Int.* **2009**, *49*, 1141–1149. [CrossRef]
75. Han, J.; Wang, X.D.; Ba, D.C. Coordinated Analysis of Multiple Factors of Argon Blowing Parameters on the effect of Circulation Flow Rate in RH Vacuum Refining Process. *Vacuum.* **2014**, *109*, 68–73. [CrossRef]
76. Zhang, Z.M.; Ma, P.; Dong, J.H.; Liu, M.; Liu, Y.G.; Lai, C.B. Effects of Different RH Degasser Nozzle Layouts on the Circulating Flow Rate. *Materials* **2022**, *15*, 8476. [CrossRef]
77. Wang, J.H.; Ni, P.Y.; Chen, C.; Ersson, M.; Li, Y. Effect of gas blowing nozzle angle on multiphase flow and mass transfer during RH refining process. *Int. J. Miner. Metall. Mater.* **2023**, *30*, 844–856. [CrossRef]
78. Wang, J.H.; Ni, P.Y.; Zhou, X.B.; Liu, Q.L.; Ersson, M.; Li, Y. Study on Multiphase Flow Characteristics During RH Refining Process Affected by Nonradial Arrangement of Gas-Blowing Nozzle. *Steel Res. Int.* **2023**, *94*, 2300200. [CrossRef]
79. Nakanishi, K.; Szekely, J.; Chang, C.W. Experimental and Theoretical Investigation of Mixing Phenomena in the RH-vacuum Process. *Ironmak. Steelmak.* **1975**, *2*, 115–124.
80. Li, X.; Wang, H.; Tian, J.; Wang, D.; Qu, T.; Hou, D.; Hu, S.; Wu, G. Investigation on the Alloy Mixing and Inclusion Removement through Using a New Slot-Porous Matched Tuyeres. *Metals* **2023**, *13*, 667. [CrossRef]
81. Ramírez-López, A. Analysis of Mixing Efficiency in a Stirred Reactor Using Computational Fluid Dynamics. *Symmetry* **2024**, *16*, 237. [CrossRef]
82. Qi, F.S.; Ye, N.; Liu, Z.G.; Cheung, S.; Li, B.K. Numerical Study on the Decarburization Processes in Vacuum-Refining Degasser Using the Population Balance Method. *Metall. Mater. Trans. B* **2025**, 1–17. [CrossRef]

Disclaimer/Publisher's Note: The statements, opinions and data contained in all publications are solely those of the individual author(s) and contributor(s) and not of MDPI and/or the editor(s). MDPI and/or the editor(s) disclaim responsibility for any injury to people or property resulting from any ideas, methods, instructions or products referred to in the content.